Eggers, J., Turkoz, E., Lopez-Herrera, J., Arnold, C., & Deike, L. (2018). Axisymmetric simulation of viscoelastic filament thinning with the Oldroyd-B model. *Journal of Fluid Mechanics*, *851*, [R2]. https://doi.org/10.1017/jfm.2018.514

Axisymmetric Simulation of Viscoelastic Filament Thinning with the Oldroyd-B Model

Emre Turkoz[1], Jose M. Lopez-Herrera[2], Jens Eggers[3], Craig B. Arnold[1], and Luc Deike[1,4]†

[1]Department of Mechanical and Aerospace Engineering, Princeton University, Princeton, NJ, 08544, USA

[2]Departamento Ing. Aerospacial y Mecanica de Fluidos, Universidad de Sevilla, Espana

[3]School of Mathematics, University of Bristol, University Walk, Bristol BS8 1TW, United Kingdom

[4]Princeton Environmental Institute, Princeton University, Princeton, NJ, 08544, USA

(Received xx; revised xx; accepted xx)

Fundamental understanding of filament thinning of viscoelastic fluids is important in practical applications such as spraying and printing of complex materials. Here, we present direct numerical simulations of the two-phase axisymmetric momentum equations using the volume-of-fluid technique for interface tracking and the log-conformation transformation to solve the viscoelastic constitutive equation. The numerical results for the filament thinning are in excellent agreement with the theoretical description developed with a slender body approximation. We show that the off-diagonal stress component of the polymeric stress tensor is important and should not be neglected while investigating the later stages of filament thinning. This demonstrates that such numerical methods can be used to study details not captured by one-dimensional slender body approximation and pave the way for numerical studies of viscoelastic fluid flows.

1. Introduction

Thinning of viscoelastic filaments and formation of drops are important for many practical applications (Basaran *et al.* 2013), ranging from the printing of silver pastes for electronics to the deposition of cells for tissue engineering. The development of accurate numerical modeling of viscoelastic flows, including filament thinning and breakup, would provide significant advances to the fundamental understanding of the physics at play and lead to the development of reproducible fabrication techniques.

A theoretical approach to investigate the viscoelastic filament thinning has been the use of a slender jet formulation which is derived using the lubrication approximation (Eggers & Villermaux 2008) coupled with the constitutive equation of the viscoelastic model. This approximation results in a one-dimensional model, consisting of an equation of motion to track the axial velocity component, u_z, an advection equation to track the filament thickness in axial direction, h, and constitutive equations to track the axial and radial components of the polymeric stress, σ_{zz} and σ_{rr}, respectively. This one-dimensional description has been used to investigate the thinning of viscoelastic filaments with a special emphasis given to the thinning of Oldroyd-B and finitely extensible nonlinear elastic (FENE) fluids (Clasen *et al.* 2006; Wagner *et al.* 2005; Ardekani *et al.* 2010). Oldroyd-B constitutive equations have attracted considerable attention earlier

† Email address for correspondence: ldeike@princeton.edu

because they exhibit the formation of the "beads-on-a-string" structure, which denotes the formation of periodic droplets attached along a filament (Li & Fontelos 2003). To fully capture this structure, the distribution of stress components at the neck region connecting the thread with the drop should be resolved in detail, which can not be accomplished using one-dimensional slender formulation because the structure of drops attached to a thin filament is not slender. Therefore, the complete equations should be simulated in an axially symmetric domain to examine the velocity and stress field throughout the filament.

Simulation of the breakup of viscoelastic filament in axially symmetric domain has been presented in Bousfield *et al.* (1986) and Étienne *et al.* (2006), where the problem can be simulated until the minimum filament thickness thins and reaches the 50% and 30% of the initial radius, respectively. The increasing stiffness of the problem prevents the simulation to proceed further in time because the Oldroyd-B model allows for the build up of an infinite stress so that the filament should not breakup as long as the numerical grid is sufficiently small. Inkjet printing process motivates the simulation of viscoelastic jets, using a coupled Lagrangian-Eulerian scheme using finite element discretization (Harlen *et al.* 1995; Morrison & Harlen 2010) and a constitutive model that allows for breakup such as FENE-P. As FENE-P, there are other constitutive models that avoid the development of infinite stresses. For instance, the Giesekus model (Hulsen *et al.* 2005) is used to represent shear-thinning polymer solutions while FENE-CR (Haward *et al.* 2012) is an empirical model that modifies the FENE-P model to separate the shear-thinning effects from the elastic effects.

The complexity of the viscoelastic filament thinning comes from the different time scales involved. The time scales to characterize the viscoelastic thinning are the relaxation time, λ, which is the time for the strain to relax when an applied stress is removed, the visco-capillary time scale, $t_v = \eta_0 R_0/\gamma$, and the inertia-capillary time scale, $t_c = \sqrt{\rho R_0^3/\gamma}$, where R_0 is the filament radius, ρ the density, γ is the surface tension with air, and $\eta_0 = \eta_s + \eta_p$ is the zero shear viscosity where η_s and η_p are solvent and polymeric viscosities, respectively. This defines two non-dimensional numbers, the Deborah number, De, and the Ohnesorge number, Oh (Bhat *et al.* 2010; Turkoz *et al.* 2018):

$$\mathrm{De} = \frac{\lambda}{t_c} = \frac{\lambda}{\sqrt{\rho R_0^3/\gamma}}, \qquad \mathrm{Oh} = \frac{t_v}{t_c} = \frac{\eta_0}{\sqrt{\rho\gamma R_0}}. \tag{1.1}$$

The Ohnesorge compares the inertia-capillary and viscous-capillary time scales. The Deborah number compares the fluid relaxation time to the flow timescale and in many cases equivalent to the Weissenberg number (Dealy 2010), $\mathrm{Wi} = \lambda\dot{\epsilon}$, where $\dot{\epsilon}$ is the strain rate. For high Deborah number flows, simulations performed with the conventional finite volume discretization of the full set of equations have suffered from the phenomenon called the high-Weissenberg number problem (Keunings 1986; Renardy 2000). This problem arises when the Oldroyd-B model is used and the stresses inside the filament continues to rise exponentially without a limit. Eventually, the numerical simulations fail in resolving these high stresses and stress gradients (Renardy 2000). Various transformations have been proposed to overcome this challenge such as the kernel-transformation (Balci *et al.* 2011) and the log-conformation (Fattal & Kupferman 2005) technique. Here, we use the log-conformation technique to overcome the high-Weissenberg number problem. This technique is based on the reformulation of the constitutive equation in terms of the matrix logarithm of the conformation tensor. According to (Fattal & Kupferman 2005), taking the matrix logarithm reduces the conformation tensor's exponential variation so that this variation can be approximated by polynomials. We also tried to use the kernel

transformation technique to solve for the polymeric stresses, however, this technique did not lead to convergence for our configuration.

The rate of thinning of viscoelastic fluids can be described as the balance of surface tension and elastic forces, with the assumption of a spatially constant and slender profile (Bazilevskii *et al.* 1997). This leads to an exponential decrease of the minimum radius of a thinning viscoelastic filament h_{min} with time (Clasen *et al.* 2006):

$$h_{min}(t) = h_0 \exp[-t/(3\lambda)], \tag{1.2}$$

where h_0 depends on initial conditions. Equation (1.2) is used to evaluate the relaxation time of viscoleasitc fluids from the time evolution of h_{min} (Anna & McKinley 2001). Therefore, an accurate numerical model should capture the exponential polymeric thinning accurately. The axial polymeric stress σ_{zz} and the velocity component can also be derived and are given by Clasen *et al.* (2006) as:

$$\sigma_{zz} = \sigma_0 \exp(t/3\lambda), \qquad \frac{\partial u_z}{\partial z} = \frac{2}{3\lambda}, \tag{1.3}$$

where σ_0 is the stress value at the beginning of the exponential thinning. Accurately capturing these relationships can be considered as a benchmark for numerical models of viscoelastic fluids.

In this paper, we examine the thinning of an Oldroyd-B type of filament by using direct numerical simulations and solving the axisymmetric, two-phase, incompressible momentum equations with surface tension using the open source solver Basilisk (Popinet 2015, 2018). The interface between the high density viscoelastic liquid and the low density ambient air is reconstructed by a volume of fluid (VOF) method, which has been validated for complex multiphase flows such as splashing (Howland *et al.* 2016), breaking waves (Deike *et al.* 2016) and bubble bursting (Deike *et al.* 2018). Here, we find that the time evolution of the thinning thread and the axial distribution of velocity and polymeric stress components along the filament follow the theoretical predictions. Also, while the one-dimensional approximation can capture the trends of stresses successfully, the off-diagonal stress component of the polymeric stress tensor is not negligible as the thinning progresses in time.

2. Numerical Simulations

We consider incompressible mass conservation and momentum equations with the addition of the polymeric stress as an extra term in the stress tensor. These equations are given by Clasen *et al.* (2006) as:

$$\nabla \cdot \mathbf{u} = 0, \tag{2.1}$$

$$\rho \left(\frac{\partial \mathbf{u}}{\partial t} + \mathbf{u} \cdot \nabla \mathbf{u} \right) = -\nabla p + \nabla \cdot \underline{\underline{\sigma}}, \tag{2.2}$$

where the total stress tensor has two components $\underline{\underline{\sigma}} = \underline{\underline{\sigma_s}} + \underline{\underline{\sigma_p}}$. The solvent viscous stress tensor has the usual definition $\underline{\underline{\sigma}}_s = 2\eta_s \underline{\underline{D}}$ where η_s is the solvent viscosity and $\underline{\underline{D}} = (\nabla \mathbf{u} + \nabla \mathbf{u}^T)/2$ is the strain-rate tensor. The polymeric stress tensor is evaluated according to the Oldroyd-B model as (Ardekani *et al.* 2010):

$$\frac{D\underline{\underline{\sigma_p}}}{Dt} = (\nabla \mathbf{u})^T \cdot \underline{\underline{\sigma_p}} + \underline{\underline{\sigma_p}} \cdot (\nabla \mathbf{u}) - \frac{1}{\lambda} \underline{\underline{\sigma_p}} + \frac{\eta_p}{\lambda} (\nabla \mathbf{u} + \nabla \mathbf{u}^T), \tag{2.3}$$

where η_p is the polymer viscosity, and λ is the relaxation time as explained in the previous section. We represent the governing parameters of filament thinning following the study

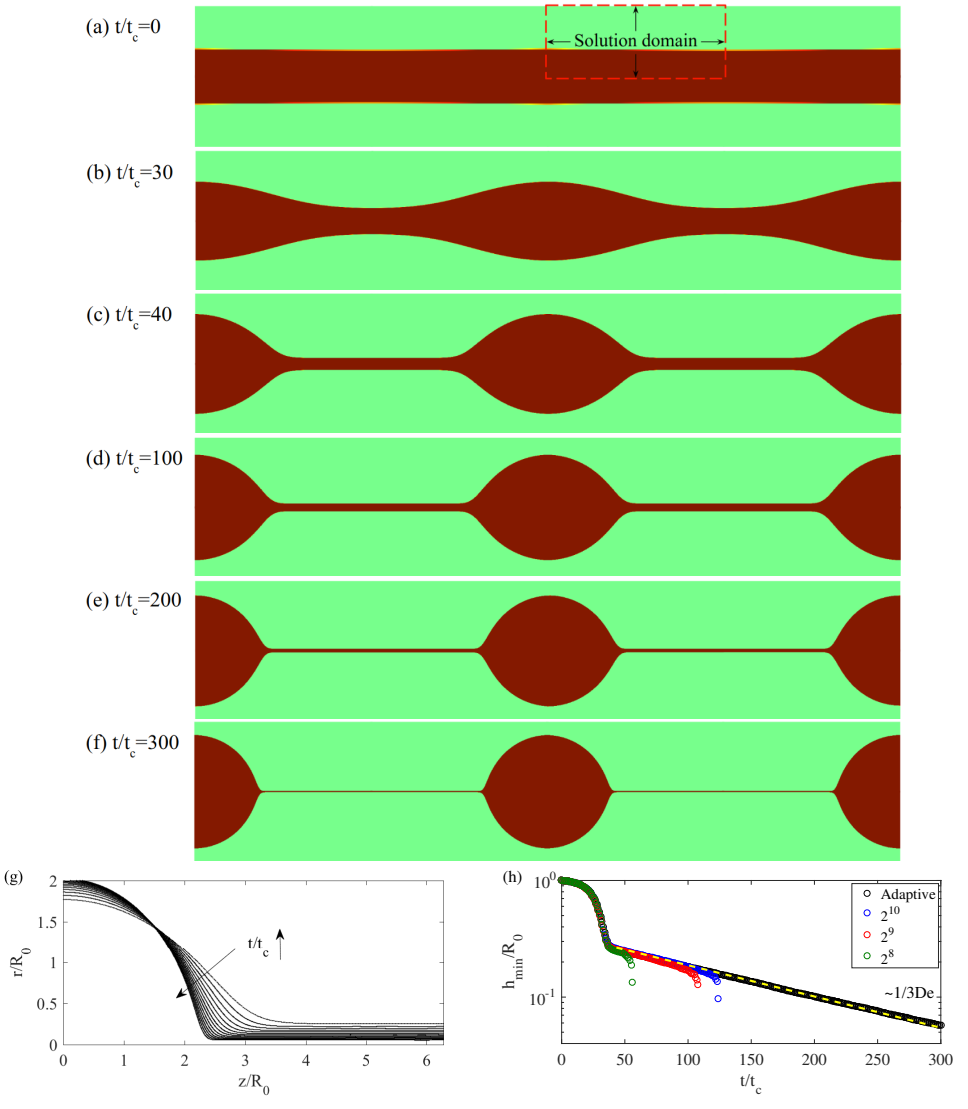

FIGURE 1. Filament thinnnig simulations results for an Oldyord-B type of fluid on an axially symmetric domain. Simulation parameters are similar to those presented in Clasen *et al.* (2006): De = 60, Oh = 3.16 and $\beta = 0.25$. (a)-(e) Snapshots of the thinning of the liquid bridge obtained by adding the interface profiles periodically at (a) $t/t_c = 0$, (b) $t/t_c = 30$, (c) $t/t_c = 40$, (d) $t/t_c = 150$ and (e) $t/t_c = 300$. The solution domain is axially symmetric and shown with the red rectangle with dashed edges in (a). Periodicity and symmetry are used to create the images. The bottom boundary is the axially symmetry axis. The left and right wall boundary conditions are symmetry boundary conditions as well. (g) Evolution of the interface between $t/t_c = 50$ and $t/t_c = 300$. The time difference between each curve is $\Delta t = 20t_c$. The neck region connecting the thread with the drop becomes steeper as the time proceeds. (h) The minimum radius of the filament as a function of time. Exponential thinning starts after $t/t_c \approx 40$. The exponential fit to the polymeric thinning shows good agreement with the theory, which states for h_{min} that $h_{min}(t)/R_0 = h_0/R_0 \exp[-t/(3\mathrm{De}t_c)]$. The exponential fit yields $h_0/R_0 = 0.30$ for De = 60 with an R-square error of 0.9968. Convergence of this thinning is observed as function of the grid size allowing to solve the thinning for longer times.

presented in Clasen *et al.* (2006). The total dynamic viscosity of the polymer solution is denoted as $\eta_0 = \eta_s + \eta_p$. An important parameter that affects the stiffness of the problem is the viscosity ratio, defined as $\beta = \eta_s/\eta_0$. As the viscosity ratio decreases, the problem becomes numerically more challenging to solve. An alternative and equivalent representation is to separate the relative dimensionless contributions of the viscosity $\nu_s = \mathrm{Oh}\beta$ for the solvent and $\nu_p = \mathrm{Oh}(1-\beta)$ for the polymer (Clasen *et al.* 2006).

In the log-conformation technique, one solves for the conformation tensor $\underline{\underline{c}}$ instead of the polymeric stress tensor as given in equation (2.3). In the Oldroyd-B model, these two tensors are related by $\underline{\underline{\sigma_p}} = \frac{\lambda}{\eta_p}(\underline{\underline{c}} - \underline{\underline{I}})$, where $\underline{\underline{I}}$ is the identity matrix, then, the equation for the conformation tensor becomes

$$\frac{\partial \underline{\underline{c}}}{\partial t} + \mathbf{u}\cdot\nabla\underline{\underline{c}} - \left(\nabla\mathbf{u}\cdot\underline{\underline{c}} + \underline{\underline{c}}\cdot\nabla\mathbf{u}^T\right) = \frac{1}{\lambda}(\underline{\underline{c}} - \underline{\underline{I}}). \tag{2.4}$$

The components of this tensor are solved using the numerical scheme presented in Hao & Pan (2007) by first taking the matrix logarithm of the conformation tensor as $\underline{\underline{\psi}} = \log\underline{\underline{c}}$. This is possible because the conformation tensor is always positive definite. The equation for $\underline{\underline{\psi}}$ is easier to solve numerically because the logarithm of the exponentially increasing polymeric stresses is resolved. After the equation is solved, the conformation tensor is evaluated as $\underline{\underline{c}} = \exp(\underline{\underline{\psi}})$. This implementation in Basilisk is described in Lopez-Herrera *et al.* (2018). An initial perturbation, ε, is introduced to initiate the capillary thinning of the filament, so that the initial filament profile $h(z,0)$ is:

$$h(z,0)/R_0 = 1 - \varepsilon\sin\left(\frac{z/R_0}{4}\right), \tag{2.5}$$

where the domain is $0 \leqslant z/R_0 \leqslant 2\pi$. The problem is defined by the non-dimensional numbers De, Oh and β introduced before, the air-liquid density and viscosity ratios, ρ_a/ρ_s and η_a/η_s, which are expected to have a small effect in the limit of large ratios.

3. Results

3.1. *Viscoelastic Filament Thinning*

The simulation is started with a liquid cylinder of initial radius R_0 and a perturbation $\epsilon = 0.05$. The non-dimensional parameters are $\mathrm{De} = 60$, $\mathrm{Oh} = 3.16$, $\beta = 0.25$, $\rho_a/\rho_s = \eta_a/\eta_s = 0.01$, which are representative of a high Deborah number liquid bridge thinning configuration. Figure 1a-f shows the time evolution of the filament, with the initially perturbed liquid bridge starting to thin (a-b) developing a rather slender filament and a drop (c-d). The thinning proceeds exponentially (e-f) with viscoelastic effects allowing for the formation of a very thin film of radius down to 5% of the initial drop (f). Figure 1g shows the time evolution of the interface from $t/t_c = 40$ to $t/t_c = 300$. The minimum filament radius h_{min} as a function of time is presented in Fig. 1h, showing an excellent agreement with the prediction given in equation (1.2), $h_{min}(t)/R_0 = (h_0/R_0)\exp[-t/(3\mathrm{De}t_c)]$. When we fit the polymeric thinning from $t/t_c = 40$ to $t/t_c = 300$, we obtain $h_0/R_0 = 0.30$ for $\mathrm{De} = 60$ with an R-square error of 0.99, in very good agreement with the theory (Clasen *et al.* 2006), where $h_0/R_0 = \mathrm{Oh}\,(1-\beta)\,/\mathrm{De} = 0.27$. These results show that our model can capture the polymeric thinning successfully and follow the theoretical prediction for the thinning. From our numerical experiments, we note that changing ρ_a/ρ_s and η_a/η_s have no observable effects on our results as long as these ratios are smaller than 0.1. Changing Oh only affects the exponential thinning starting time with larger Oh delaying the thinning due to viscous

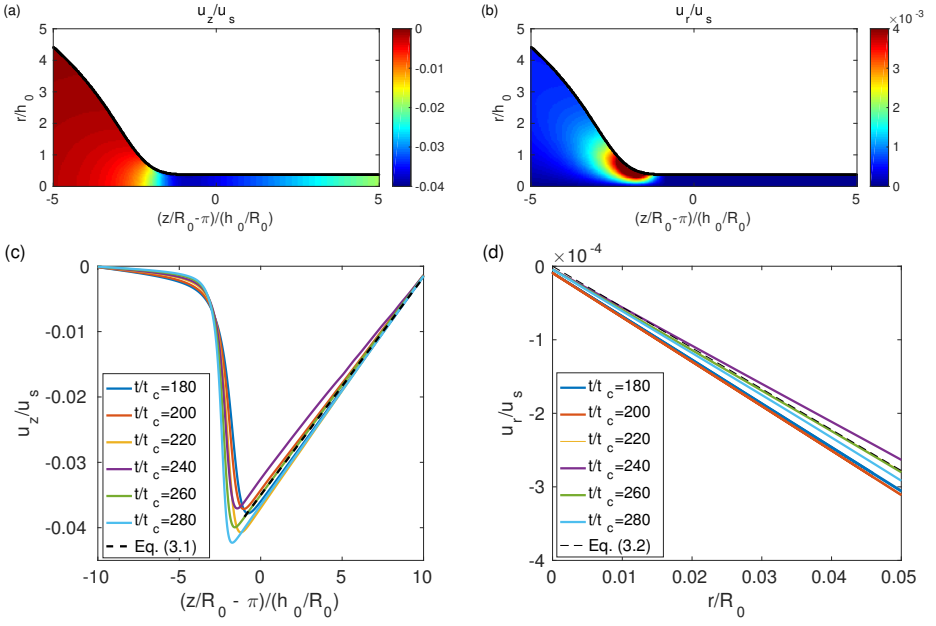

FIGURE 2. Dimensionless axial and radial velocity components from our simulations, where the length scale is normalized by the filament radius and the time scale is normalized by the capillary time scale $t_c = \sqrt{\rho R_0^3/\gamma}$ so that the velocity scale is $u_s = R_0/t_c$. (a) Colormap of the axial velocity component u_z/u_s at $t/t_c = 180$ as a representative case. An axial flux is directed towards the drop from the thinning thread, and this flux results in the growth of the drop while the connected filament thins. The radial change of axial velocity inside the thread can be neglected so that $\partial u_z/\partial r \approx 0$. (b) Colormap of the radial velocity component u_r/u_s at $t/t_c = 180$ as a representative case. The radial velocity has a maximum at the interface where the filament is connected to the drop. The axial change of the radial velocity can be neglected inside the thread, $\partial u_r/\partial z \approx 0$. (c) Axial velocity component along $r/R_0 = 0$ at different times. The linear part corresponding to the thinning thread has the slope of $2\dot{\zeta}$ at all times as the plotted theory line. (d) Radial velocity component along $z/R_0 = 2\pi$ at different time steps. This component should have the slope of $-\dot{\zeta}$ at all times as the plotted theory line.

effects. We also note that decreasing β increases the stiffness of the problem, and when β is reduced, the initial part of the thinning becomes faster (due to the smaller solvent viscosity) before the exponential thinning starts.

The independence of the filament thinning with the grid size is shown in Fig. 1h. Three fixed grids with 2^8, 2^9 and 2^{10} grid points along one edge of the square domain (of length 2π) are shown to collapse together with the adaptive scheme which uses functions that refine the grid according to the numerical error in velocity and the curvature in both axial and radial directions. We see that the adaptive scheme yields to the same results at early time steps with the uniform 2^{10} grid, and a higher refinement is required at later times when the filament thins significantly because the thinning reaches a width close to the mesh size. The adaptive scheme refines the grid up to 2^{12}, which allows the simulations to reach later time steps, and we can capture the thinning up to 5.0% of the initial radius with at least 40 grid points along the thin filament in radial direction.

The axial and radial velocity components are important to understand the filament thinning. Figure 2a and 2b show the normalized velocity fields u_z/u_s and u_r/u_s, respectively, as a function of the normalized length scale $(z/R_0 - \pi)/(h_0/R_0)$ and $(r/R_0)/(h_0/R_0)$ with $u_s = R_0/t_c$ at $t/t_c = 180$. Figure 2a shows that there is an axial

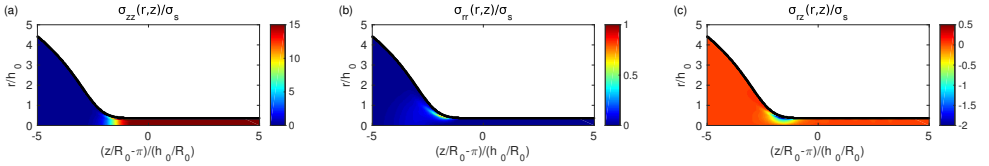

FIGURE 3. Colormaps of the polymeric stress components at $t/t_c = 180$ as a representative case that shows the typical distribution of stresses: (a) The axial component σ_{zz}/σ_s. (b) The radial component σ_{rr}/σ_s. (c) The off-diagonal component σ_{rz}/σ_s. We observe that the axial stress has the largest magnitude. We also see that σ_{rz} is actually significant and it can not be neglected compared to σ_{rr} while remaining small compared to σ_{zz}.

flux directed towards the drop from the filament, which results in the growth of the drop while the connected filament thins. This figure also shows that the radial change of axial velocity inside the thread can be neglected so that $\partial u_z/\partial r \approx 0$. Figure 2b shows that the radial velocity is maximum at the neck region where the filament is connected to the drop. Similarly, inside the polymeric thinning region, the axial change of the radial velocity can be neglected, $\partial u_r/\partial z \approx 0$.

The axial velocity along the axial direction ($r/R_0 = 0$) in the filament is presented in Fig. 2c, while the radial velocity along the radial direction ($z/R_0 = 2\pi$) in the filament is shown in Fig. 2d. As shown in Clasen *et al.* (2006), using the continuity equation, the axial velocity component along the thread is equal to:

$$u_z(r, z, t)/u_s = 2\dot{\zeta} z/R_0 + u_{z,0}, \tag{3.1}$$

where $u_{z,0} = -4\pi\dot{\zeta}$ so the axial velocity at the center of the filament ($z/R_0 = 2\pi$) connecting two beads is equal to zero. The radial velocity component is:

$$u_r(r, z, t)/u_s = -\dot{\zeta} r/R_0, \tag{3.2}$$

where $\dot{\zeta} = 1/3\mathrm{De}$ is the coefficient for the slope. The velocity profiles obtained numerically are following the theoretical predictions given by equations (3.1) and (3.2) closely as shown in Fig. 2c and Fig. 2d, respectively.

Now, we examine the polymeric stress components σ_{zz}, σ_{rr} and σ_{rz} during the exponential thinning. The one-dimensional slender body approximation does not account for σ_{rz} in the formulation of the equation of motion (Clasen *et al.* 2006). In addition, the one-dimensional formulation predicts the dimensionless axial stress to vary as $\sigma_{zz}/\sigma_s = \sigma_0/\sigma_s \exp(t/3\mathrm{De}t_c)$, where $\sigma_s = \rho u_s^2$ is the characteristic stress scale. The stress components at a representative time during the exponential thinning are presented in Fig. 3, and indicate that σ_{rz} can not be neglected compared to σ_{rr}. This result is significant because the one-dimensional lubrication approximation does not take σ_{rz} into account due to the formulation of the slender jet equations. We also note that the distribution of σ_{rz} and σ_{rr} are very similar with their maxima in magnitude around the neck region.

The axial stress component σ_{zz} is shown as a function of the rescaled axial direction $(z/R_0 - \pi)/(h_0/R_0)$ along $r/R_0 = 0$ for different time steps in Fig. 4a. We see that the axial stress maintains a flat profile inside the thinning thread over time, while the stress inside the drop is negligible. This means that as the thinning thread supplies the attached drop with more material, a growing stress has to be supported by the thread itself to sustain the integrity of the structure. The change of the axial stress inside the filament as a function of time during the polymeric thinning is shown in Fig. 4b and is found to follow the theoretical prediction, with $\sigma_0/\sigma_s = 5.83$ evaluated in the simulation for $\mathrm{De} = 60$ with an R-square error of 0.98. This value is close to the predicted $\sigma_0/\sigma_s = 2/(h_0/R_0) = 6.66$ from the one-dimensional modeling (Clasen *et al.* 2006).

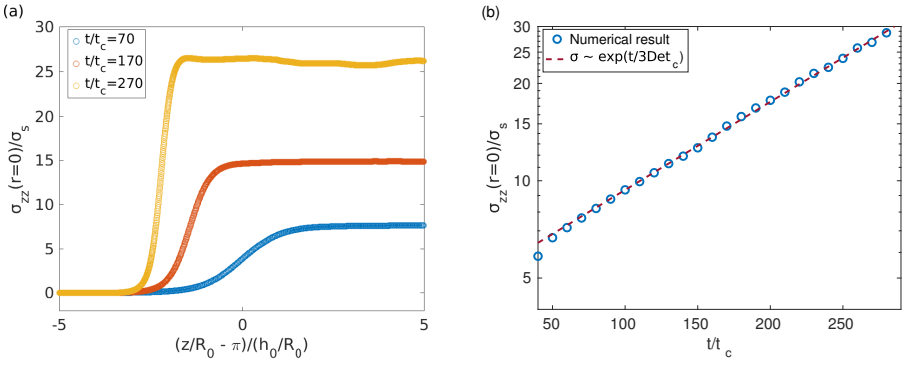

FIGURE 4. Evolution of the axial stress component σ_{zz} along the filament. (a) σ_{zz}/σ_s as a function of the rescaled axial location $(z/R_0 - \pi)/h_0$ at different times. σ_{zz} is constant along the filament as predicted by the slender body approximation. The stress gradient between the drop and the thread becomes larger as the filament thins. (b) σ_{zz}/σ_s at $r/R_0 = 0$ as a function of time. The stress increases exponentially with time, $\sigma_{zz}(z,t)/\sigma_s = \sigma_0/\sigma_s \exp(t/3\mathrm{De}t_c)$, with the fitted value, $\sigma_0/\sigma_s = 5.83$ for $\mathrm{De} = 60$ with an R-square error of 0.99.

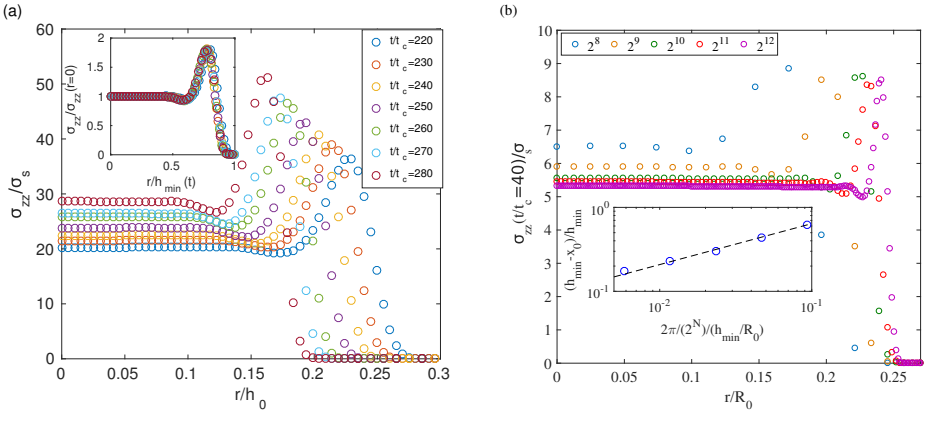

FIGURE 5. Radial distribution of the polymeric axial stress σ_{zz}. (a) σ_{zz}/σ_s as a function of the scaled radial coordinate r/h_0 along the filament. The stress goes to zero beyond the interface with the ambient air. The stress profile exhibits similarity so that all data can be rescaling into a single curve by $\sigma_{zz}(r/R_0 = 0)/\sigma_s$ and $r/h_{min}(t)$ (inset). (b) Grid size dependence of the stress profile (evaluated at $t/t_c = 40$). As the number of grid point 2^N is increased, the peak stress location is pushed towards the interface and the size of the bump is getting smaller. The inset shows that the normalized bump size $(h_{min} - x_0)/h_{min}$ descreases as the grid size increases $(2\pi/2^N)/(h_{min}/R_0)$ where x_0 denotes the distance where the stress starts to deviate from the uniform value measured from the center $r = 0$. Dashed line is a power-law fit $1.97x^{-0.50}$.

3.2. *Polymeric Axial Stress Profile*

Figure 5a shows the distribution of σ_{zz} as a function of the rescaled radial direction r/h_0 at different times, and we observe a peculiar profile. As the time proceeds, the peak stress and the stress at $r = 0$ increase exponentially, and the peak stress location shifts towards the symmetry axis as the filament thins. We show in the inset of Fig. 5a, by rescaling the axial stress component along the interface with the stress at $r = 0$, $\sigma_{zz,r=0}$ and the radial coordinate with the interface thickness at that time, $r/h_{min}(t)$, so that $r/h_{min} = 1$ denotes the interface, that the radial distribution of the stress is similar in time where the ratio of the peak stress to the stress at the center of the filament is

preserved along with the size of the stress bump. We note that this profile is similar to the "boundary layer stress profile" at stretching viscoelastic filament simulations presented in the literature (Yao & McKinley 1998).

The radial distribution of the polymeric axial stress depicted in Fig. 5a is unexpected. We investigate the width of the non-uniform region and the magnitude of the peak stress change with the grid size. Figure 5b shows the results at the time step $t/t_c = 40$ for increasing grid size, with 2^N the number of grid points along the filament in the axial direction (N from 8 to 12). The time $t/t_c = 40$ is chosen because it is after the polymeric thinning starts and before the 2^8 grid filament breaks up. The width of the non-uniform stress region decreases with increasing refinement and the peak stress location is pushed towards the filament-air interface. The normalized non-uniform stress bump width $(h_{min} - x_0)/h_{min}$ as a function of grid size, $2\pi/(2^N)/h_{min}$, at time $t/t_c = 40$ is shown in Fig. 5d, where x_0 is the he distance where the stress starts to deviate from the uniform value measured from the center $r = 0$. We see that the width of the non-uniform stress region as a function of the normalized grid size decreases according to a power-law relationship with a coefficient of -0.5. As the grid size increases, the bump width gets smaller with an unchanged peak stress value, suggesting that the bump would become infinitely thin as the resolution keeps increasing with a peak value that does not depend on the resolution. While this grid dependent polymeric axial stress structure, which might be a numerical artifact, is observed, it does not have an apparent effect on the evolution of the minimum filament thinning and velocity components, which are excellent agreement with the predictions presented in equations (1.2) and (1.3).

3.3. *Self-similar Profile and Comparison with Experiments*

We compare our numerical results for the interface profiles with the experimental data presented in Clasen *et al.* (2006) in Fig. 6, showing r/h_{min} as a function of $(z - z_0)/h_{min}$, for the final stages of the thinning. The numerical profiles are plotted for every $10t/t_c$ intervals from $t/t_c = 220$ to $t/t_c = 300$, with z_0 the numerically determined axial location of the maximum radial velocity. We observed that while both the numerical and experimental profiles present a clear self-similar dynamics, the slopes of the experimental profiles turn out to be steeper than the slopes of the numerical results as discussed for the one-dimensional modeling (Clasen *et al.* 2006).

3.4. *Simulating the Beads-on-a-string Structure*

Our numerical model can be used for the canonical beads-on-a-string structure, as an example for possible applications. We consider parameters within the range of existence of beads-on-a-string (Wagner *et al.* 2005), and studied using a one-dimensional model with parameters by Ardekani *et al.* (2010), Oh = 0.04, De = 0.8, $\beta = 0.27$, and an initial sinusoidal perturbation $\epsilon = 0.05$. We obtain the expected beads-on-a-string structure with two large drops connected with a satellite droplet as shown in Fig. 7a-d. The aspect ratio of the satellite to the large droplet is found to be similar to previous one-dimensional work (Ardekani *et al.* 2010). We also show the distribution of the axial velocity u_z/u_s in Fig. 7e. It is seen that the filament thins while the fluxes are directed towards both the satellite and the main drops.

4. Conclusions

We present direct numerical simulations of the two-phase axisymmetric momentum equations for viscoelastic thinning of an Oldroyd-B fluid, and employ the log-conformation technique to overcome the high-Weissenberg number problem. The

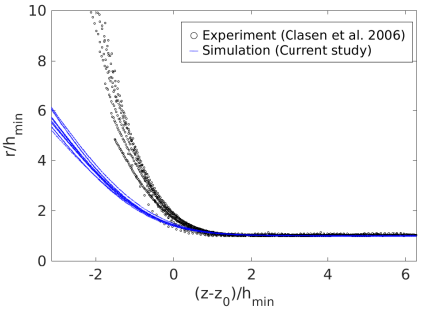

FIGURE 6. Self-similar thinning obtained from the present simulation and the experimental data from Clasen *et al.* (2006), for a liquid bridge with $R_0 = 3$ mm, $\gamma = 37$ mN m^{-1}, $\rho = 1026$ kg m^{-3}, solvent viscosity $\eta_s = 65.2$ Pa s, polymeric viscosity $\eta_p = 9.8$ Pa s and the relaxation time $\lambda = 8.1$ s. The last 9 experimental profiles taken in intervals of 0.5 s are shown, and rescaled by h_{min} measured experimentally. Numerical results for every $10t/t_c$ time steps from $t/t_c = 220$ to $t/t_c = 300$, with z_0 the location where the radial velocity component is maximum, and h_{min} determined numerically. Both numerical and experimental data present a self-similar evolution with time but experimental data are much sharper.

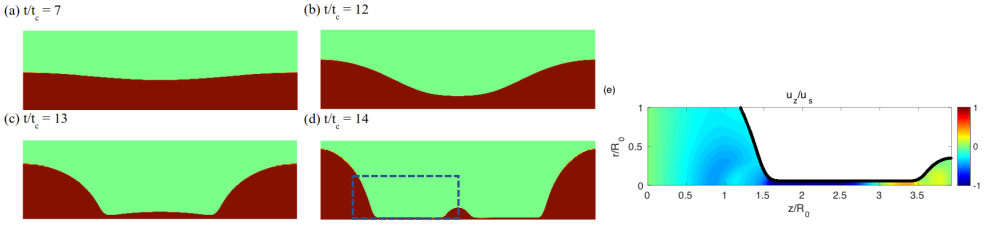

FIGURE 7. The beads-on-a-string structure simulated with the two-dimensional model in axially symmetric domain. (a-d) Snapshots of the thinnnig liquid bridge that results in the satellite drop formation at (a) $t/t_c = 7$, (b) $t/t_c = 12$, (c) $t/t_c = 13$, (d) $t/t_c = 14$. (e) Colormap of the axial velocity component u_z/u_s at $t/t_c = 14$, within the area shown by the dashed line in (d). Inside the filament there are fluxes towards both the large and the small drops.

thinning of the filament, and its velocity as a function of time is successfully modeled and can be described by the one-dimensional theory derived from slender body approximations. The polymeric stress components of the thinning filament are examined and the off-diagonal stress component σ_{rz} is not negligible while it is not taken into account by one-dimensional formulations. Furthermore, the axial stress component σ_{zz} exhibits a self-similar radial distribution in time. This structure exhibits a grid-dependent properties while not having an apparent effect on the outcome of the simulation results in terms of the velocity and filament thinning. Note that using the Oldroyd-B model, we did not capture the blistering instability observed experimentally on stretched viscoelastic filaments (Chang *et al.* 1999; Sattler *et al.* 2008), which may require the implementation of an extension of the Oldroyd-B model (Eggers 2014) to solve for the polymer and solvent phases inside the filament separately. With this study, we demonstrate the ability to perform simulations of complex two-dimensional viscoelastic flows which opens the way for the development of viscoelastic models for real-life applications.

Acknowledgements

We are grateful to Stephane Popinet and Wouter Mostert for discussions about viscoelastic simulations using Basilisk. Computations were partially performed using al-

location TGOCE140023 to L.D. from the Extreme Science and Engineering Discovery Environment (XSEDE), supported by NSF Grant No. ACI-1053575. J.E. acknowledges support from the Leverhulme Trust through International Academic Fellowship IAF-2017-010. This work is also supported by National Science Foundation (NSF) through a Materials Research Science and Engineering Center (MRSEC) program (DMR-1420541).

REFERENCES

Anna, S. L. & McKinley, G. H. 2001 Elasto-capillary thinning and breakup of model elastic liquids. *Journal of Rheology* **45** (1), 115–138.

Ardekani, A. M., Sharma, V. & McKinley, G. H. 2010 Dynamics of bead formation, filament thinning and breakup in weakly viscoelastic jets. *J. Fluid. Mech.* **665**, 46–56.

Balci, N., Thomases, B., Renardy, M. & Doering, C. R. 2011 Symmetric factorization of the conformation tensor in viscoelastic fluid models. *J. Non-Newtonian Fluid Mech.* **166** (11), 546–553.

Basaran, O. A., Gao, H. & Bhat, P. P. 2013 Nonstandard inkjets. *Ann. Rev. Fluid Mech.* **45**, 85–113.

Bazilevskii, A. V., Entov, V. M., Lerner, M. M. & Rozhkov, A. N. 1997 Failure of polymer solution filaments. *Polymer Science Series Vysokomolekuliarnye Soedineniia* **39**, 316–324.

Bhat, P. P., Appathurai, S., Harris, M. T., Pasquali, M., McKinley, G. H. & Basaran, O. A. 2010 Formation of beads-on-a-string structures during break-up of viscoelastic filaments. *Nature Physics* **6** (8), 625–631.

Bousfield, D. W., Keunings, R., Marrucci, G. & Denn, M. M. 1986 Nonlinear analysis of the surface tension driven breakup of viscoelastic filaments. *Journal of Non-Newtonian Fluid Mechanics* **21** (1), 79–97.

Chang, H.-C., Demekhin, E. A. & Kalaidin, E 1999 Iterated stretching of viscoelastic jets. *Physics of Fluids* **11** (7), 1717–1737.

Clasen, C., Eggers, J., Fontelos, M. A., Li, J. & McKinley, G. H. 2006 The beads-on-string structure of viscoelastic threads. *J. Fluid Mech.* **556**, 283–308.

Dealy, J. M. 2010 Weissenberg and Deborah numbers – their definition and use. *Rheolegy Bulletin* **79** (2), 14–18.

Deike, L., Ghabache, E., Liger-Belair, G., Das, A. K, Zaleski, S., Popinet, S. & Séon, T. 2018 Dynamics of jets produced by bursting bubbles. *Phys. Rev. Fluids* **3** (1), 013603.

Deike, L., Melville, W. K. & Popinet, S. 2016 Air entrainment and bubble statistics in breaking waves. *J. Fluid Mech.* **801**, 91–129.

Eggers, J 2014 Instability of a polymeric thread. *Physics of Fluids* **26** (3), 033106.

Eggers, J. & Villermaux, E. 2008 Physics of liquid jets. *Reports on Progress in Physics* **71** (3), 036601.

Étienne, J., Hinch, E. J. & Li, J. 2006 A Lagrangian–Eulerian approach for the numerical simulation of free-surface flow of a viscoelastic material. *J. Non-Newtonian Fluid Mech.* **136** (2-3), 157–166.

Fattal, R. & Kupferman, R. 2005 Time-dependent simulation of viscoelastic flows at high Weissenberg number using the log-conformation representation. *J. Non-Newtonian Fluid Mech.* **126** (1), 23–37.

Hao, J. & Pan, T.-W. 2007 Simulation for high Weissenberg number: viscoelastic flow by a finite element method. *Applied Mathematics Letters* **20** (9), 988–993.

Harlen, O. G., Rallison, J. M. & Szabo, P. 1995 A split Lagrangian–Eulerian method for simulating transient viscoelastic flows. *J. Non-Newtonian Fluid Mech.* **60** (1), 81–104.

Haward, S. J., Oliveira, M.S.N., Alves, M. A & McKinley, G. H. 2012 Optimized cross-slot flow geometry for microfluidic extensional rheometry. *Physical Review Letters* **109** (12), 128301.

Howland, C. J., Antkowiak, A., Castrejón-Pita, J. R., Howison, S. D., Oliver, J. M., Style, R. W. & Castrejón-Pita, A. A. 2016 It's harder to splash on soft solids. *Phys. Rev. Lett.s* **117** (18), 184502.

Hulsen, M. A., Fattal, R. & Kupferman, R. 2005 Flow of viscoelastic fluids past a cylinder

at high Weissenberg number: stabilized simulations using matrix logarithms. *Journal of Non-Newtonian Fluid Mechanics* **127** (1), 27–39.

Keunings, R. 1986 On the high Weissenberg number problem. *J. Non-Newtonian Fluid Mech.* **20**, 209–226.

Li, J. & Fontelos, M. A. 2003 Drop dynamics on the beads-on-string structure for viscoelastic jets: A numerical study. *Physics of Fluids* **15** (4), 922–937.

Lopez-Herrera, J.M, Popinet, S. & Castrejón-Pita, A. A. 2018 An adaptive solver for viscoelastic incompressible two-phase problems applied to the study of the splashing of slightly viscoelastic droplets. *Submitted* .

Morrison, N. F. & Harlen, O. G. 2010 Viscoelasticity in inkjet printing. *Rheologica acta* **49** (6), 619–632.

Popinet, S. 2015 A quadtree-adaptive multigrid solver for the Serre–Green–Naghdi equations. *Journal of Computational Physics* **302**, 336–358.

Popinet, S. 2018 Numerical models of surface tension. *Ann. Rev. Fluid Mech.* **50** (1), 49–75.

Renardy, M. 2000 Asymptotic structure of the stress field in flow past a cylinder at high Weissenberg number. *J. Non-Newtonian Fluid Mech.* **90** (1), 13–23.

Sattler, R, Wagner, C & Eggers, J 2008 Blistering pattern and formation of nanofibers in capillary thinning of polymer solutions. *Physical Review Letters* **100** (16), 164502.

Turkoz, E., Perazzo, A., Kim, H., Stone, H. A. & Arnold, C. B. 2018 Impulsively induced jets from viscoelastic films for high-resolution printing. *Phys. Rev. Lett.s* **120** (7), 074501.

Wagner, C., Amarouchene, Y., Bonn, D. & Eggers, J. 2005 Droplet detachment and satellite bead formation in viscoelastic fluids. *Phys. Rev. Lett.s* **95** (16), 164504.

Yao, M & McKinley, G. H. 1998 Numerical simulation of extensional deformations of viscoelastic liquid bridges in filament stretching devices. *Journal of Non-Newtonian Fluid Mechanics* **74** (1-3), 47–88.